SU(3) fermions in a three-band graphene-like model

Ankur Das[1] and Sumiran Pujari[2]
[1]*Department of Physics and Astronomy, University of Kentucky, Lexington, Kentucky 40506, USA*
[2]*Department of Physics, Indian Institute of Technology Bombay, Mumbai, MH 400076, India*

(Received 5 July 2019; published 23 September 2019)

Two-dimensional graphene is fascinating because of its unique electronic properties. From a fundamental perspective, one among them is the geometric phase structure near the Dirac points in the Brillouin zone, owing to the SU(2) nature of the Dirac cone wave functions. We ask if there are geometric phase structures in two dimensions which go beyond that of a Dirac cone. Here we write down a family of three-band continuum models of noninteracting fermions which have more intricate geometric phase structures. This is connected to the SU(3) nature of the wave functions near threefold degeneracies. We also give a tight-binding free fermion model on a two-dimensional graphene-like lattice where the threefold degeneracies are realized at fine-tuned points. Away from them, we obtain new "three-band" Dirac cone structures with associated nonstandard Landau level quantization, whose organization is strongly affected by the non-SU(2) or beyond-Dirac geometric phase structure of the fine-tuned points.

DOI: 10.1103/PhysRevB.100.125152

I. INTRODUCTION

Geometric phases and related concepts have proved invaluable in understanding quantum mechanical phenomena which depend on the analytic structure of a parametrized Hilbert space, ranging from magnetoelectric phenomena to topological insulators [1,2]. Another striking domain is the quantum Hall effect that has been very instructive to modern condensed matter [2]. For weakly correlated electrons, they manifest in the Hilbert space of the Bloch wave functions of a band solid, where the parameter is the reciprocal crystal momentum. Berry phase is routinely used to quantify such geometric phases [3]. There are other quantifiers as well, e.g., the famous TKNN invariant is used in integer quantum Hall effect to quantify the geometric phase structure of filled gapped bands [4].

A very familiar example of a Berry phase effect in two dimensions (2D) is that of graphene [5]. The Dirac cone spectra associated with monolayer graphene has a nontrivial geometric phase structure for each cone. Specifically, there is a Berry phase of $e^{i\pi}$ when one circuits around the cone. In the presence of magnetic field and consequent Landau level formation, this structure can manifest sometimes as new Hall conductance plateaus [6]. Multilayer graphene [7] is another example that hosts other multiples of π Berry phases around its Dirac-like degeneracies.

For the above examples, there is an argument going back to Berry's original article [3] that shows why we get multiples of π (or equivalently, half-integral multiples of 2π). When one considers the most general Hamiltonian that can characterize any twofold degeneracy as happens in Dirac-like degeneracies, one obtains a SU(2) matrix $H = \sum_{i\in\{1,2,3\}} \lambda_i \hat{\sigma}_i$ [8]. The geometric phase in this case, is half the solid angle subtended by the circuit in the parameter space at the degeneracy point. Since in the preceding we have in general three parameters, for a non-fine-tuned degeneracy as a function of 2D crystal momentum in a 2D Bloch Hamiltonian, we need symmetries to reduce down to two parameters [9]. Once so restricted to two parameters, we can only get multiples of π. This is the usual Dirac-like geometric phase structure in two dimensions.

The above argument motivates the starting point of this paper. Can there be two-dimensional noninteracting electronic band structures that host non-Dirac geometric phase structures? Since we have just argued that this possibility is absent for twofold degeneracies, we have to look beyond them. The simplest generalization can then be a threefold degeneracy. Thus we start by writing down a natural three-band generalization of the Dirac cone continuum Hamiltonian [Eq. (3)]. We find that this particular generalization indeed hosts a more intricate geometric phase structure than the twofold Dirac cone wave functions. Even at the level of the spectrum, there are twofold line degeneracies that emanate from the threefold degenerate point in the parameter space. Because of these line degeneracies, and thereby a lack of adiabaticity in the usual sense [3], computing Berry phase around the threefold degeneracy is formally problematic [10].

This leads us to describe this geometric phase structure using a triplet of indices which tracks how many times each member of the triplet (parameter, the Hamiltonian, the eigenfunctions) individually winds back to themselves as the system winds back to itself once, as we keep circuiting around the degeneracy point. Here, by the system, we mean the collection of the parameters, the Hamiltonian, and all eigenfunctions. For our purpose, it proves useful to employ this method to classify the geometric phase structure near a multifold degenerate point in 2D especially in the presence of line degeneracies. This quantifier may be thought of as a conceptual generalization of the pseudospin winding number [11].

Analyzing this toy model further from the point of view of what space symmetries can give rise to this kind of a threefold degeneracy, we find an interesting SU(3) group structure near the threefold degeneracy. It turns out that the above mentioned

beyond-Dirac-like geometric phase structure is obtained at fine-tuned points. Away from them, we get novel three-band Dirac-cone spectra that are a consequence of being "adiabatically" connected to this kind of threefold degeneracy that we have found. We go on to write a tight-binding model which is hosted on a hexagonal lattice similar to graphene but with three basis sites per unit cell. This still preserves the SU(3) structure near threefold degenerate points, now with an additional valley index arising similar to graphene. Curiously the twofold line degeneracies mentioned before connect the two valleys on a noncontractible loop in the Brillouin zone.

As a contrast to the toy model introduced above, we consider another simple three-band generalization of the Dirac cone as in Eq. (5) with a threefold degeneracy. For this case, one again finds a Dirac-like geometric phase structure. This kind of threefold degeneracy can be thought of as being in the spin-1 representation of SU(2), which is again why we get Berry phases that are multiples of π. Thus, the SU(3) structure of our toy model is intimately related to its non-Dirac-like geometric phase structure. Classifying nontrivial multifold degeneracies in an electronic band structure as representations of certain groups (constrained by space symmetries) is a powerful point of view [12,13]. In 2D there are several works which have considered threefold degeneracies. Green *et al.* [14] considered band structures resulting from putting microscopic fluxes in the hexagonal and Kagome lattices where they found a threefold degeneracy. Here the fermions are in the spin-1 representation of the SU(2) group, but their primary motivation was to find flat band structures. Subsequently, many other cases of spin-1 SU(2) threefold degeneracies have been reported [15–23]. Reference [19]'s α-$\mathcal{T}_3$ model on the Dice lattice is noteworthy because it accommodates an interpolation between spin-$\frac{1}{2}$ and spin-1 Dirac fermions. We also note that in 3D, which is not our focus, threefold degeneracies have garnered tremendous interest recently, where they have been sometimes dubbed as triple point fermions [24–35]. All these cases correspond to fermions being in the spin-1 representation of SU(2) in the majority (however, see Ref. [29] for an example where the geometric phase structure goes beyond Weyl/Dirac in 3D).

In our 2D toy model, unlike the above, the fermions are in the fundamental representation of the SU(3) group. Going away from this fine-tuned model, we get multiple twofold Dirac cones for generic directions and a threefold point degeneracy for some fine-tuned directions. But the SU(3) nature of the toy model manifests itself in the way the various twofold and threefold degeneracies are organized to accommodate the SU(3) geometric phase structure. Thus, the presence of the fine-tuned SU(3) point controls the various Dirac cone structures obtained in its vicinity.

The outline of the paper is as follows: In Sec. II we write down a three-band generalization of the Dirac cone Hamiltonian, and discuss its beyond-Dirac geometric phase structure. In Sec. III we study the construction of such generalizations using symmetries. This gives a family of three-band Hamiltonians where the fermions transform in the fundamental representation of SU(3). In Sec. III B we categorize the band structures for various cases of this family of Hamiltonians. In Sec. IV we give a lattice model realization of the above Hamiltonians, and a brief numerical study of the effect of uniform magnetic field on this noninteracting system. We conclude with a summary and outlook in Sec. V.

II. THREE-BAND CONSTRUCTION

To set the stage, we recall that the low-energy physics of graphene is obtained from a two-band lattice hopping model [5,36] which gives two distinct Dirac cones or valleys in the Brillouin zone of the underlying triangular Bravais lattice. Our convention is to choose the location of valleys as $\mathbf{K} = (\frac{4\pi}{3}, 0)$ and $\mathbf{K}' = (-\frac{4\pi}{3}, 0)$ (unit length is set by separation between two neighboring unit cells, and $\mathbf{K}$, $\mathbf{K}'$ are related by a reflection across the y axis). Near one of these valleys in energy units of $\hbar v_F = 1$, one can write down the familiar continuum Hamiltonian

$$H_K^{\text{Dirac}}(\mathbf{p}) = \begin{pmatrix} 0 & p_x - ip_y \\ p_x + ip_y & 0 \end{pmatrix}, \tag{1}$$

where $\mathbf{p}$ is the expansion variable near $\mathbf{K}$ with the full crystal momentum being $\mathbf{K} + \mathbf{p}$. Its eigensystem is

$$\begin{aligned} \epsilon_1(\mathbf{p}) &= +p\,; \quad v_1(\mathbf{p}) = \frac{1}{\sqrt{2}}(e^{-i\theta_{\mathbf{p}}}, 1)^T, \\ \epsilon_2(\mathbf{p}) &= -p\,; \quad v_2(\mathbf{p}) = \frac{1}{\sqrt{2}}(-e^{-i\theta_{\mathbf{p}}}, 1)^T, \end{aligned} \tag{2}$$

where $p = \sqrt{p_x^2 + p_y^2}$ and $\theta_{\mathbf{p}} = \arctan(\frac{p_y}{p_x})$. This gives the familiar Berry phase of $e^{i\pi}$ as the parameter $\mathbf{p}$ (and thereby the angular variable $\theta_{\mathbf{p}}$) winds around once about the twofold degenerate point. We note here that during this winding, the full system—comprising the parameter $\mathbf{p}$, the Hamiltonian $H_K^{\text{Dirac}}(\mathbf{p})$, and all eigenvectors $\{v_i(\mathbf{p})\}$—winds around once as well.

Now we come to our primary object of interest in this paper. Consider the following three-band generalization of the continuum Dirac Hamiltonian $H_K^{\text{Dirac}}(\mathbf{p})$ recalled above,

$$H_K^{3A}(\mathbf{p}) = \begin{pmatrix} 0 & p_x - ip_y & p_x - ip_y \\ p_x + ip_y & 0 & p_x + ip_y \\ p_x + ip_y & p_x - ip_y & 0 \end{pmatrix}, \tag{3}$$

where the subscript K refers again to a valley index anticipating the lattice model realization of the above in Sec. IV. The eigensystem of $H_K^{3A}(\mathbf{p})$ is

$$\epsilon_1^{3A}(\mathbf{p}) = -2p\cos\left(\frac{\theta_{\mathbf{p}} + \pi}{3}\right),$$

$$v_1^{3A}(\mathbf{p}) = \frac{1}{\sqrt{3}}(\omega^2 e^{-i\frac{2\theta_{\mathbf{p}}}{3}} \quad \omega\, e^{i\frac{2\theta_{\mathbf{p}}}{3}} \quad 1)^T, \tag{4a}$$

$$\epsilon_2^{3A}(\mathbf{p}) = 2p\cos\left(\frac{\theta_{\mathbf{p}}}{3}\right),$$

$$v_2^{3A}(\mathbf{p}) = \frac{1}{\sqrt{3}}(e^{-i\frac{2\theta_{\mathbf{p}}}{3}} \quad e^{i\frac{2\theta_{\mathbf{p}}}{3}} \quad 1)^T, \tag{4b}$$

$$\epsilon_3^{3A}(\mathbf{p}) = -2p\cos\left(\frac{\theta_{\mathbf{p}} - \pi}{3}\right),$$

$$v_3^{3A}(\mathbf{p}) = \frac{1}{\sqrt{3}}(\omega\, e^{-i\frac{2\theta_{\mathbf{p}}}{3}} \quad \omega^2 e^{i\frac{2\theta_{\mathbf{p}}}{3}} \quad 1)^T, \tag{4c}$$

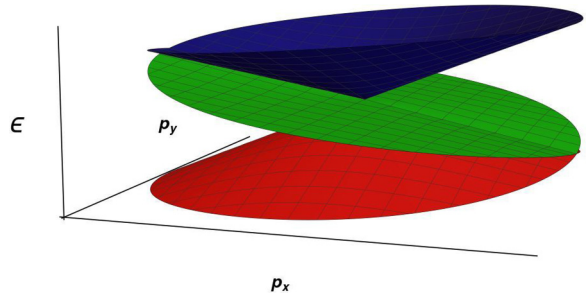

FIG. 1. The dispersion for H_K^{3A} [Eq. (3)].

where $\omega = e^{i\frac{2\pi}{3}}$, $\omega^2 = e^{-i\frac{2\pi}{3}}$ are the complex cube roots of unity.

The dispersion near the threefold degeneracy is shown in Figs. 1 and 2 (for fixed $p = 1$). It is linear in p similar to a Dirac cone, however, now there are a pair of twofold line degeneracies that emanate from the threefold degeneracy outwards in the opposite directions along the p_x axis. This already gives us a sense of the non-Dirac geometric phase structure of H_K^{3A}.

The source of the non-Dirac geometric phase structure actually lies in the $e^{i\theta_{\mathbf{p}}/3}$ and $e^{i2\theta_{\mathbf{p}}/3}$ terms in H_K^{3A}'s eigensystem Eq. (4). The analytic structure of these terms is qualitatively different than $e^{i\theta_{\mathbf{p}}}$ that appears in the eigensystem of H_K^{Dirac}. $z = re^{i\theta}$ is an analytic function everywhere on the complex plane, whereas $z^{1/3} = r^{1/3}e^{i\theta/3}$ has branch cuts in the complex plane, and needs three Riemann surfaces to embed the function in an analytic way. The twofold line degeneracies in Fig. 1 are representing these branch cuts in the following way: we can rewrite the eigenvalues as $\{\epsilon_1^{3A}(\mathbf{p}) = 2p\,\mathrm{Re}[\omega^2\sqrt[3]{e^{i\theta_{\mathbf{p}}}}], \epsilon_2^{3A}(\mathbf{p}) = 2p\,\mathrm{Re}[\sqrt[3]{e^{i\theta_{\mathbf{p}}}}], \epsilon_3^{3A}(\mathbf{p}) = 2p\,\mathrm{Re}[\omega\sqrt[3]{e^{i\theta_{\mathbf{p}}}}]\}$ which are essentially the Riemann surfaces of the complex cube root. We also show this in a different way in Fig. 2 through pairs of colored arrows which indicate the rule to move among the bands across the line degeneracies in order to move in an analytically smooth way.

To quantify the geometric phase structure of H_K^{3A}, we cannot use Berry phase straightforwardly due to the line degeneracies which present obstructions while doing a circuit in the parameter space around the threefold degeneracy. However, from the above discussion, we see that to move in an analytically smooth way, we have moved across bands as shown in Fig. 2 as we make circuits around the threefold degeneracy. This figure also shows that to analytically return back to the starting point in energy (modulo p) at a nondegenerate point, we have to circuit three times around the degeneracy. During these three circuits, one may easily check that the Hamiltonian [Eq. (3)] returns back to itself thrice as well, while the wave functions return back to themselves only *twice* via Eq. (4).

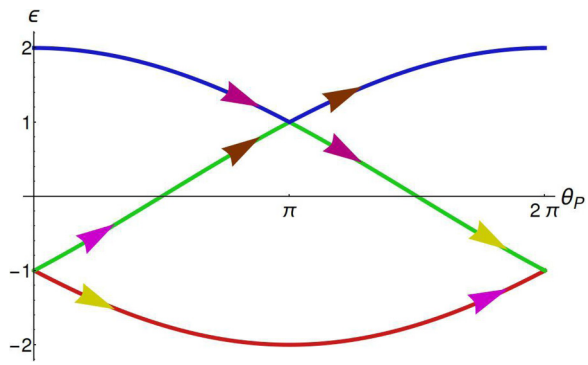

FIG. 2. The dispersion for H_K^{3A} [Eq. (3)] at a constant magnitude of momentum ($p = 1$) about $\mathbf{p} = (0, 0)$ [see Eq. (4)]. The arrows are a guide to move across the bands in a smooth way, where the rule is to follow the same colored arrows while crossing the line degeneracies.

TABLE I. This table represents different band structures and their classification using the triplet of indices introduced in the main text: (t) → top, (m) → middle, (b) → bottom. QBT below refers to quadratic band touching relevant for bilayer graphene [7], whose continuum Hamiltonian near a valley may be written as $\begin{pmatrix} 0 & (p_x - ip_y)^2 \\ (p_x + ip_y)^2 & 0 \end{pmatrix}$. The first three cases are Dirac-like with the first two of them being twofold cases, while the third case is a threefold case. The very last case is beyond Dirac-like.

Bands	Model	$\theta_{\mathbf{p}}$	H	v_i
2	Dirac	1	1	1(t), 1(b)
	QBT	1	2	2(t), 2(b)
3	H_K^{3B}	1	1	1(t), 2 (m), 1(b)
	H_K^{3A}	3	3	2(t), 2 (m), 2(b)

This motivates the following triplet of indices to characterize the geometric phase structure around any two-dimensional multifold degeneracy. We track how many times the parameter ($\theta_{\mathbf{p}}$), the given Hamiltonian, and all eigenfunctions $v^i(\theta_{\mathbf{p}})$ return to themselves, as we perform a single circuit around the degeneracy for the full system comprising the parameter, the Hamiltonian, and all eigenvectors. This triplet of indices tracking the individual windings is a quantifier of the geometric phase structure near the degeneracy. This is summarized in Table I for several different twofold and threefold degenerate systems. We see from this table how our three-band model has a nontrivially different geometric phase structure than the other cases which are all Dirac-like. Thus our model is an example of a beyond-Dirac geometric phase structure in two dimensions. It can also be checked that $\begin{pmatrix} 0 & p_x - ip_y & p_x - ip_y \\ p_x + ip_y & 0 & p_x - ip_y \\ p_x + ip_y & p_x + ip_y & 0 \end{pmatrix}$ has the same kind of beyond-Dirac geometric phase structure as H_K^{3A}.

Our three-band continuum Hamiltonian can be contrasted with a Dirac-like three-band case with a threefold degeneracy of the following form:

$$H_K^{3B}(\mathbf{p}) = \begin{pmatrix} 0 & p_x + ip_y & 0 \\ p_x - ip_y & 0 & p_x + ip_y \\ 0 & p_x - ip_y & 0 \end{pmatrix}. \tag{5}$$

Its eigensystem is

$$\epsilon_1^{3B}(\mathbf{p}) = -\sqrt{2}p,$$
$$v_1^{3B}(\mathbf{p}) = \begin{pmatrix} \frac{1}{2}e^{-2i\theta_{\mathbf{p}}} & -\frac{e^{-i\theta_{\mathbf{p}}}}{\sqrt{2}} & \frac{1}{2} \end{pmatrix}^T, \tag{6a}$$

$$\epsilon_2^{3B}(\mathbf{p}) = 0,$$
$$v_2^{3B}(\mathbf{p}) = \left(-\frac{e^{-2i\theta_\mathbf{p}}}{\sqrt{2}} \quad 0 \quad \frac{1}{\sqrt{2}}\right)^T, \tag{6b}$$
$$\epsilon_3^{3B}(\mathbf{p}) = \sqrt{2}p,$$
$$v_3^{3B}(\mathbf{p}) = \left(\frac{1}{2}e^{-2i\theta_\mathbf{p}} \quad \frac{e^{-i\theta_\mathbf{p}}}{\sqrt{2}} \quad \frac{1}{2}\right)^T. \tag{6c}$$

As is evident from the eigensystem above, this case has no branch cut structure and no line degeneracies. It can, in fact, be shown that the geometric phase structure, in this case, is still Dirac-like similar to H_K^{Dirac} but in a threefold situation [37]. We also note how it contrasts with beyond-Dirac-like H_K^{3A} in Table I. In all of the above, we have fixed our gauge by choosing the last entry of the wave functions' column vectors to be purely real. The classification in Table I is independent of this gauge choice, since wave functions differing by pure phases are physically equivalent and have the same windings around degeneracies.

III. SU(3) GROUP STRUCTURE

In this section we expose the underlying SU(3) group structure in Eq. (3) as remarked in Sec. I. To set the stage, we remind ourselves that for monolayer graphene with twofold degeneracies, a continuum Hamiltonian can be written using the Pauli matrices [SU(2) generators in fundamental representation] near the degeneracy points in the Brillouin zone. It is obtained by expanding around the $\mathbf{K}$ and $\mathbf{K}'$ points in the Brillouin zone of graphene and looks like

$$\mathcal{H}^{\text{Dirac}} = \sum_{\mathbf{p}} \hat{c}^\dagger_{\mu\alpha}(\mathbf{p})\, H^{\text{Dirac}}_{\mu\alpha,\mu'\alpha'}\, \hat{c}_{\mu\alpha}(\mathbf{p}), \tag{7}$$

where $\hat{c}^\dagger_{\mu\alpha}$, $\hat{c}_{\mu\alpha}$ are the fermion creation and annihilation operators for the so-called valley index $\mu \in \mathbf{K}, \mathbf{K}'$ and sublattice index $\alpha \in a, b$,

$$H^{\text{Dirac}}_{\mu\alpha,\mu'\alpha'} = p_x\left(\tau^3_{\mu\mu'} \otimes \sigma^1_{\alpha\alpha'}\right) + p_y\left(\tau^0_{\mu\mu'} \otimes \sigma^2_{\alpha\alpha'}\right), \tag{8}$$

and τ^i are SU(2) Pauli matrices indexing the two valleys, σ^i are SU(2) Pauli matrices indexing the two sublattices of the graphene lattice, $\mathbf{p}$ is the expansion variable (i.e., the full crystal momentum is $\mathbf{k} = \mathbf{K} + \mathbf{p}$, etc.), and all the indices have been shown explicitly. We can rewrite Eq. (8) concisely by dropping the explicit indices as $H^{\text{Dirac}} = p_x(\tau^3 \otimes \sigma^1) + p_y(\tau^0 \otimes \sigma^2)$. In this way of saying, our three-band continuum Hamiltonian written down in the previous section in Eq. (3) actually requires *all* the off-diagonal generators of the SU(3) group, i.e.,

$$H_K^{3A}(\mathbf{p}) = p_x(\Lambda_1 + \Lambda_4 + \Lambda_6) + p_y(\Lambda_2 + \Lambda_5 - \Lambda_7), \tag{9}$$

where we use the Gell-Mann matrices as the SU(3) generators [38]. On the other hand, spin-1 generators of the SU(2) group—which are a subset of the SU(3) group generators—suffice for the Hamiltonian in Eq. (5),

$$\mathcal{H}^K_{3\text{B}}(\mathbf{p}) = p_x(\Lambda_1 + \Lambda_6) + p_y(\Lambda_2 + \Lambda_7). \tag{10}$$

A. Symmetry analysis

This leads us to ask the following question: Along with time-reversal symmetry, what are the spatial point group symmetries that we want to preserve while constructing a general continuum Hamiltonian in two dimensions which has the above SU(3) group structure? In the case of graphene, the spatial point group symmetries of $\mathcal{C}_3$ ($2\pi/3$ rotation about the center of a hexagonal plaquette), $\mathcal{C}_2$ (inversion, or equivalently a π rotation about the center of a hexagonal plaquette), and $\mathcal{P}_x/\mathcal{P}_y$ (reflections about axes passing through the center of a hexagonal plaquette) are sufficient to constrain us in writing down Eq. (8) as the general continuum Hamiltonian that preserves these symmetries.

For our model, we will start by considering a $\mathcal{C}_2$ symmetry. The generic operation of the $\mathcal{C}_2$ can be taken to be as follows: one sublattice remain unchanged, while the other two sublattices get interchanged (e.g., $a \to b$, $b \to a$, $c \to c$). This operation thus looks like

$$\mathcal{C}_2 \hat{c}_{\mu\alpha}(\mathbf{p}) \mathcal{C}_2^{-1} = \left[\tau^1_{\mu\mu'} \otimes C_{2_{\alpha\alpha'}}\right] \hat{c}_{\mu'\alpha'}(-\mathbf{p}), \tag{11}$$

where

$$C_2 = \left(\Lambda^1 - \frac{\Lambda^8}{\sqrt{3}} + \frac{\Lambda^0}{3}\right) = \begin{pmatrix} 0 & 1 & 0 \\ 1 & 0 & 0 \\ 0 & 0 & 1 \end{pmatrix} \tag{12}$$

and we stick with $a \to b$, $b \to a$, $c \to c$ convention as in the example above. However this choice is not special, and all other conventions—that interchange two sublattices and keep one sublattice unchanged—will give us the same spectrum. $\mathbf{p} \to -\mathbf{p}$ in the above because the full crystal momentum changes sign, i.e., $\mathbf{k} = \mathbf{K} + \mathbf{p} \to -\mathbf{k} = -\mathbf{K} - \mathbf{p} = \mathbf{K}' - \mathbf{p}$, which is essentially the τ^1 operation in the valley index, and $\mathbf{p} \to -\mathbf{p}$ for the fermion operators.

We can easily check the following identities for the C_2 matrix ($= C_2^{-1}$) that implements $\mathcal{C}_2$,

$$C_2 \Lambda^1 C_2 = \Lambda^1, \tag{13a}$$
$$C_2 \Lambda^2 C_2 = -\Lambda^2, \tag{13b}$$
$$C_2 \Lambda^3 C_2 = -\Lambda^3, \tag{13c}$$
$$C_2(\Lambda^4 \pm \Lambda^6) C_2 = \pm(\Lambda^4 \pm \Lambda^6), \tag{13d}$$
$$C_2(\Lambda^5 \pm \Lambda^7) C_2 = \pm(\Lambda^5 \pm \Lambda^7), \tag{13e}$$
$$C_2 \Lambda^8 C_2 = \Lambda^8. \tag{13f}$$

At the outset, the list of possible terms are of the form $f_{ij}(\mathbf{p})\, \tau^i \otimes \Lambda^j$ where $f_{ij}(\mathbf{p})$ is some real function of $\mathbf{p}$. For local Hamiltonians, we can remove terms in this list which contain τ^1 or τ^2. So the generic local Hamiltonian that is invariant under $\mathcal{C}_2$ must be a combination from a reduced list of terms, e.g., terms that contain Λ^1 will be of the form

$$f^+(\mathbf{p})\, \tau^0 \otimes \Lambda^1 \quad \text{and} \quad f^-(\mathbf{p})\, \tau^3 \otimes \Lambda^1, \tag{14}$$

where the superscripts are used to designate whether the function is even or odd, i.e., $f^\pm_{ij}(-\mathbf{p}) = \pm f^\pm_{ij}(\mathbf{p})$. We quickly discuss the reason that governs the even/odd property of the above functional coefficients $f^-(\mathbf{p})$ and $f^+(\mathbf{p})$. This is a standard argument that is used for graphene as well. We will do it for the case of $\tau^0 \otimes \Lambda^1$ as an example.

Under $\mathcal{C}_2$ we have $\tau^0 \to \tau^0$. Thus using Eq. (13a), $\tau^0 \otimes \Lambda^1 \to \tau^0 \otimes \Lambda^1$. Then (from here on, we suppress indices unless needed)

$$\begin{aligned}\mathcal{C}_2\mathcal{H}^{3A}\mathcal{C}_2^{-1} &= \sum_{\mathbf{p}} \hat{c}^\dagger(-\mathbf{p}) f^+(\mathbf{p})(\tau^0 \otimes \Lambda^1)\hat{c}(-\mathbf{p}) \\ &\quad \text{(changing dummy indices as } \mathbf{p}' = -\mathbf{p}) \\ &= \sum_{\mathbf{p}'} \hat{c}^\dagger(\mathbf{p}') f^+(-\mathbf{p}')(\tau^0 \otimes \Lambda^1)\hat{c}(\mathbf{p}'). \end{aligned} \tag{15}$$

Thus $\mathcal{H}^{3A}$ remains invariant if $f^+(-\mathbf{p}) = f^+(\mathbf{p})$. All the other possible terms can be analyzed in a similar way. The full list of terms that are finally allowed by $\mathcal{C}_2$ following the above considerations are

$$\begin{aligned} &f^+(\mathbf{p})\,\tau^0 \otimes \Lambda^1, \quad f^-(\mathbf{p})\,\tau^3 \otimes \Lambda^1, \\ &g^-(\mathbf{p})\,\tau^0 \otimes \Lambda^2, \quad g^+(\mathbf{p})\,\tau^3 \otimes \Lambda^2, \\ &h^-(\mathbf{p})\,\tau^0 \otimes \Lambda^3, \quad h^+(\mathbf{p})\,\tau^3 \otimes \Lambda^3, \\ &l_1^+(\mathbf{p})\,\tau^0 \otimes (\Lambda^4 + \Lambda^6), \quad l_1^-(\mathbf{p})\,\tau^3 \otimes (\Lambda^4 + \Lambda^6), \\ &l_2^-(\mathbf{p})\,\tau^0 \otimes (\Lambda^4 - \Lambda^6), \quad l_2^+(\mathbf{p})\,\tau^3 \otimes (\Lambda^4 - \Lambda^6), \\ &m_1^+(\mathbf{p})\,\tau^0 \otimes (\Lambda^5 + \Lambda^7), \quad m_1^-(\mathbf{p})\,\tau^3 \otimes (\Lambda^5 + \Lambda^7), \\ &m_2^-(\mathbf{p})\,\tau^0 \otimes (\Lambda^5 - \Lambda^7), \quad m_2^+(\mathbf{p})\,\tau^3 \otimes (\Lambda^5 - \Lambda^7), \\ &n^+(\mathbf{p})\,\tau^0 \otimes \Lambda^8, \quad n^-(\mathbf{p})\,\tau^3 \otimes \Lambda^8. \end{aligned} \tag{16}$$

All odd functions in $\mathbf{p}$ at leading order will be linear in p_x, p_y, and all even functions in $\mathbf{p}$ at leading order will be constants. We are mainly interested in these leading order behaviors. We will comment on higher order terms when needed.

Next, we consider time reversal symmetry $\mathcal{T}$. Time reversal operation looks like

$$\mathcal{T}\hat{c}(\mathbf{p})\mathcal{T}^{-1} = [\tau^1 \otimes \Lambda^0]\hat{c}(-\mathbf{p}) \tag{17}$$

(and $\mathcal{T}\, i\, \mathcal{T}^{-1} = -i$). The list of terms allowed by time reversal symmetry (following the same steps as $\mathcal{C}_2$) are

$$\begin{aligned} &f^+(\mathbf{p})\,\tau^0 \otimes \Lambda^1, \quad f^-(\mathbf{p})\,\tau^3 \otimes \Lambda^1, \\ &g^-(\mathbf{p})\,\tau^0 \otimes \Lambda^2, \quad g^+(\mathbf{p})\,\tau^3 \otimes \Lambda^2, \\ &l_1^+(\mathbf{p})\,\tau^0 \otimes (\Lambda^4 + \Lambda^6), \quad l_1^-(\mathbf{p})\,\tau^3 \otimes (\Lambda^4 + \Lambda^6), \\ &m_2^-(\mathbf{p})\,\tau^0 \otimes (\Lambda^5 - \Lambda^7), \quad m_2^+(\mathbf{p})\,\tau^3 \otimes (\Lambda^5 - \Lambda^7), \\ &n^+(\mathbf{p})\,\tau^0 \otimes \Lambda^8, \quad n^-(\mathbf{p})\,\tau^3 \otimes \Lambda^8. \end{aligned} \tag{18}$$

Finally, we consider reflection symmetries, $\mathcal{P}_x$ about y axis and $\mathcal{P}_y$ about x axis. Their combined operations implements $\mathcal{C}_2$ in two dimensions, i.e., $\mathcal{P}_x\mathcal{P}_y = \mathcal{C}_2$. Now we know from Eq. (11) that $\mathcal{C}_2$ implements both τ^1 (valley exchange) *and* C_2 ($a \leftrightarrow b$, $c \leftrightarrow c$). So the nontrivially different symmetry operations that $\mathcal{P}_x/\mathcal{P}_y$ can do are that one of them implements valley exchange, and the other implements C_2. Also, we note that under $\mathcal{P}_x$, $\mathbf{K} \leftrightarrow \mathbf{K}'$ and under $\mathcal{P}_y$, $\mathbf{K}/\mathbf{K}'$ remain unchanged for our choice of the valley locations in the Brillouin zone. Therefore, $\mathcal{P}_x$ implements valley exchange with the sublattices unchanged, and $\mathcal{P}_y$ implements C_2 with the valleys unchanged. Thus, $\mathcal{P}_x/\mathcal{P}_y$ operations look like

$$\mathcal{P}_x\hat{c}(\mathbf{p})\mathcal{P}_x^{-1} = [\tau^1 \otimes \Lambda^0]\hat{c}(\mathcal{P}_x(\mathbf{p})), \tag{19a}$$

$$\mathcal{P}_y\hat{c}(\mathbf{p})\mathcal{P}_y^{-1} = [\tau^0 \otimes C_2]\hat{c}(\mathcal{P}_y(\mathbf{p})). \tag{19b}$$

Also, because $\mathcal{P}_x(\mathbf{k}) = (-k_x, k_y)$ and $\mathbf{K} \leftrightarrow \mathbf{K}'$ under $\mathcal{P}_x$, therefore $\mathcal{P}_x(\mathbf{p}) = (-p_x, p_y)$ as well. Similarly, $\mathcal{P}_y(\mathbf{p}) = (p_x, -p_y)$.

Now we explicitly redo the similar analysis as for $\mathcal{C}_2$ for one term $g^+(\mathbf{p})\tau^3 \otimes \Lambda^2$ as an example:

$$\begin{aligned}\mathcal{P}_x\mathcal{H}^{3A}\mathcal{P}_x^{-1} &= \sum_{\mathbf{p}} -\hat{c}^\dagger(\mathcal{P}_x(\mathbf{p}))g^+(\mathbf{p})(\tau^3 \otimes \Lambda^2)\hat{c}(\mathcal{P}_x(\mathbf{p})) \\ &\quad \text{[changing dummy indices as } \mathbf{p}' = \mathcal{P}_x(\mathbf{p})] \\ &= \sum_{\mathbf{p}'} -\hat{c}^\dagger(\mathbf{p}')g^+(\mathcal{P}_x(\mathbf{p}'))(\tau^3 \otimes \Lambda^2)\hat{c}(\mathbf{p}). \end{aligned} \tag{20}$$

Thus at the leading order $g^+(\mathbf{p})$ will be zero, but higher order terms such $p_x p_y$ will satisfy the relation $g^+(\mathcal{P}_x(\mathbf{p})) = -g^+(\mathbf{p})$ and are thus allowed. Similarly $m_2^+(\mathbf{p})$ is zero at leading order. Therefore, all the terms in Eq. (18) in principle are allowed by reflections, but restricting up to leading order, the Hamiltonian looks like

$$\begin{aligned} H = \; & p_x\,\tau^3 \otimes [f^-\Lambda^1 + l_1^-(\Lambda^4 + \Lambda^6) + n^-\Lambda^8] \\ & + p_y\,\tau^0 \otimes [g^-\Lambda^2 + m_2^-(\Lambda^5 - \Lambda^7)] \\ & + \tau_0 \otimes [f^+\Lambda^1 + n^+\Lambda^8 + l_1^+(\Lambda^4 + \Lambda^6)]. \end{aligned} \tag{21}$$

In the above, all the function symbols are now replaced by constants. This Hamiltonian for $n^- = n^+ = f^+ = l_1^+ = 0$ and $f^- = l_1^- = g^- = m_2^- \neq 0$ is Eq. (3). As discussed in Sec. II, Eq. (3) has a threefold degeneracy and two twofold line degeneracies emanating from it (see Fig. 1).

B. Various band structures

In this subsection we categorize the finer details of various band structures that result from Eq. (21). For the momentum independent terms in Eq. (21): (1) since Λ^8 is diagonal, this must come from a staggered potential contribution. If we assume that all orbitals on a, b, c sites are the same, then (like graphene) we can set this term to zero ($n^+ = 0$). The first four cases below correspond to this choice. The final case considers what happens when $n^+ \neq 0$. (2) The Λ_1, Λ_4, Λ_6 are off-diagonal. Thus $l_1^+ \neq f^+$ implies a difference in the ab and ac, bc hoppings (within an unit cell). We can measure this deformation in hopping strengths with respect to ab hopping strength, i.e., f^+ may be set to 0 without loss of generality.

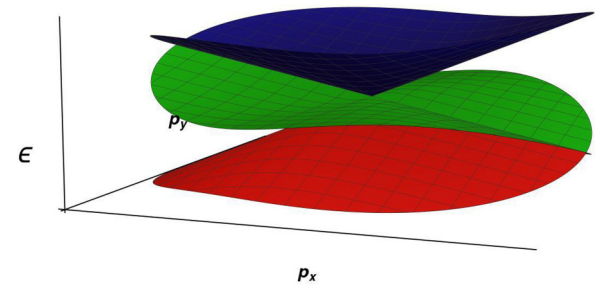

FIG. 3. Case 1: $l_1^+ = 0, n^- = 0, f^- = l_1^-$ In the above, $g^- \neq f^-$ and $m_2^- \neq l_1^-$. When all of these quantities are equal to each other, we obtain the special case as in Fig. 1 corresponding to our starting point H_K^{3A}.

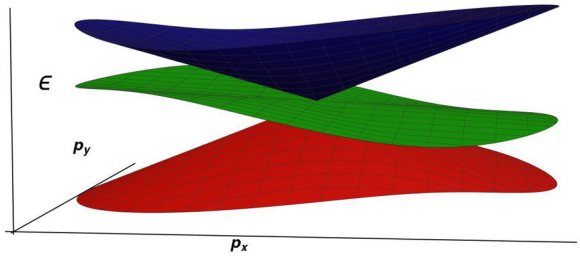

FIG. 4. Case 2: Representative picture of the effect of $f^- \neq l_1^-$ and/or $n^- \neq 0$ for $l_1^+ = 0$.

Case 1 ($l_1^+ = 0, n^- = 0, f^- = l_1^-$). This is the base case with twofold line degeneracies along $p_y = 0$, and threefold degenerate point at $p_x = p_y = 0$. See Fig. 3.

Case 2 [$l_1^+ = 0$ AND ($n^- \neq 0$ OR $f^- \neq l_1^-$)]. The line degeneracies now go away, and we end up with only one three-band degenerate point (see Fig. 4). [We note here that this corresponds to the triplet of indices 1 ($\theta_{\mathbf{p}}$), 1 (H) and 2(t), 0(m), 2(b).]

Case 3a ($l_1^+ \neq 0$, $n^- = 0$, $f^- = l_1^-$). This is shown in Fig. 5. Here the top and middle bands touch each other linearly at two points, while the middle and bottom bands touch each other linearly at one point. For the top two bands, the line connecting the degeneracy point is completely flat.

Case 3b ($l_1^+ \neq 0$, $n^- = 0$, $f^- \neq l_1^-$). Here the top and middle bands touch each other linearly at two points (similar to case 3a), while the middle and bottom bands also touch each other linearly at two points. Contrasting this with case 3a, we see that the effect of $f^- \neq l_1^-$ is to produce two Dirac cones when there was only one twofold degeneracy before. This tells us that the twofold degeneracy in case 3a is not a standard Dirac cone [39]. For the top two bands, the line connecting the degeneracy point is completely flat. As the difference between f^- and l_1^- becomes larger, then one of the two Dirac cones goes away rather quickly (see Fig. 6).

Case 4 ($l_1^+ \neq 0$, $n^- \neq 0$). The diagonal momentum dependent term $n^-\tau^3 \otimes \Lambda^8$ comes from same sublattice hoppings. The effect of this is shown in Fig. 7. We see that for strong enough n^- the three-band problem becomes an effective two-band problem with two Dirac cones connecting the top and middle bands, while the bottom band is independent. For small n^- on the other hand, there are two Dirac cones connecting middle and bottom bands as well. n^-_{cric} depends on other parameters in a detailed way which we do not concern ourselves with.

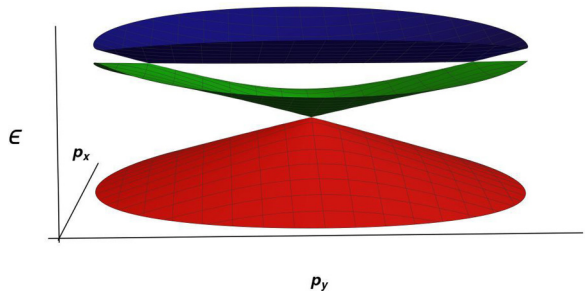

FIG. 5. Case 3a: $l_1^+ \neq 0 n^- = 0$, $f^- = l_1^-$.

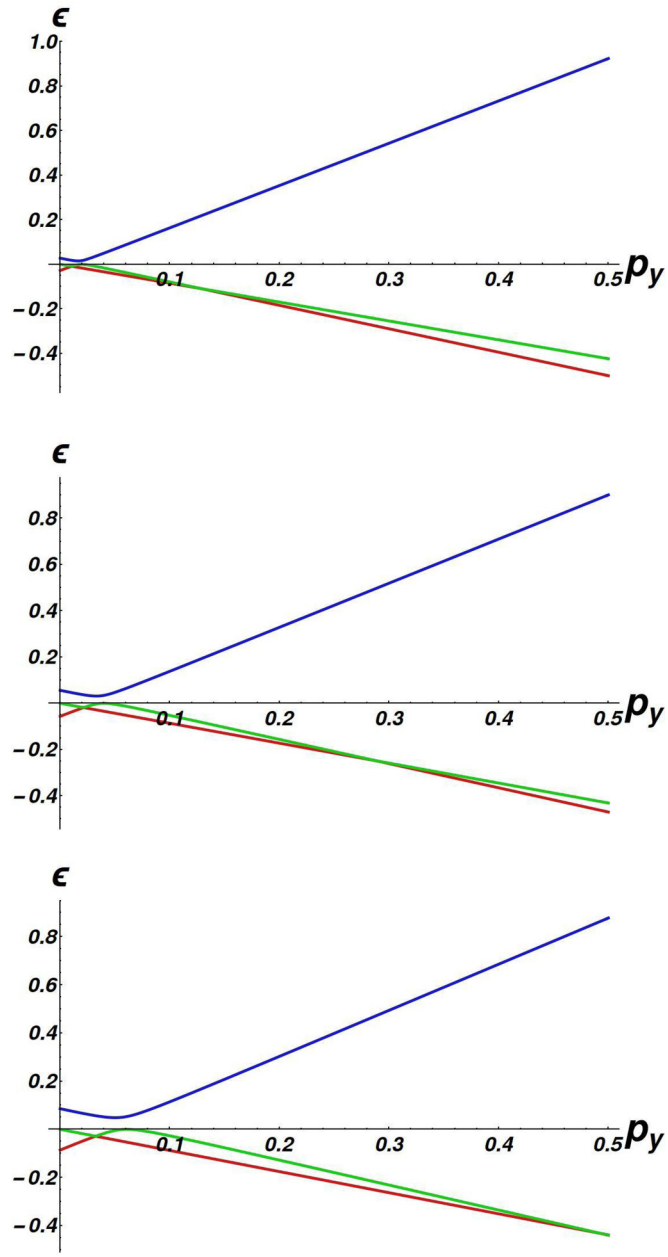

FIG. 6. Case 3b: $l_1^+ \neq 0$, $n^- = 0$, $f^- \neq l_1^-$. The three pictures are in increasing order in the difference between f^- and l_1^-.

Case 5 ($n^+ \neq 0$). When the diagonal momentum independent term $n^+\tau^0 \otimes \Lambda^8$ becomes nonzero, it effectively renders the Hamiltonian into a sum of twofold bands and a standalone band. This effect is shown in Fig. 8. This may be thought of as similar to the effect of a (sublattice) mass term in graphene due to different chemical potentials on the two sublattices. However, $n^+\tau^0 \otimes \Lambda^8$ is allowed by $\mathcal{C}_2$ symmetry, whereas different chemical potentials in graphene is forbidden by $\mathcal{C}_2$ symmetry.

The effect of g^- and m_2^- is innocuous in the preceding cases, and the above categorization goes through. We reiterate that all purely point-degenerate band touchings above have expected Berry phase windings that are $\pm\pi$, or their multiples as in the exception of case 3a which is similar to bigraphene [40].

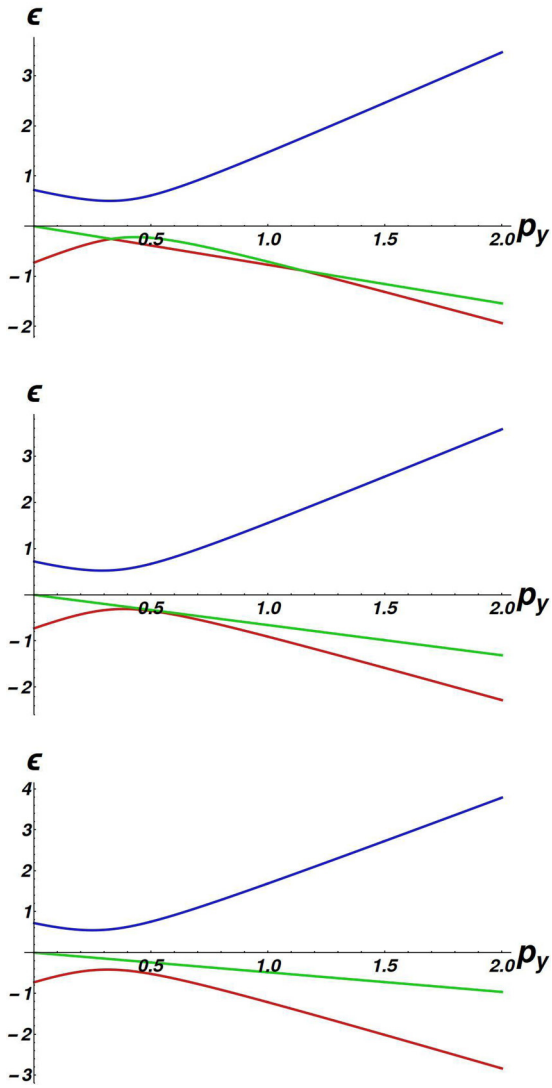

FIG. 7. Case 4 ($l_1^+ \neq 0$, $n^- \neq 0$): First picture is for $n^- < n^-_{\text{cric}}$. Second picture is for $n^- = n^-_{\text{cric}}$. The third plot is when $n^- > n^-_{\text{cric}}$ and bottom two band gap out.

IV. LATTICE MODEL

In this section we write down a graphene-like lattice fermion model motivated by the plausibility of realizing the continuum Hamiltonians described in previous sections, Eqs. (3) and (21), in some real-world material. The lattice that we consider is shown in Fig. 9. It is chosen to be very similar to the graphene lattice with an extra lattice site in the middle of vertical bonds. On this lattice, apart from the conventional hopping matrix elements as in graphene between a to b sublattices, we also include hopping matrix elements between a and c sublattices as well as b and c sublattices. We note that the geometric distance between a-c and between b-c inside the same unit cell is smaller than between a-b. For interunit cell hoppings, the situation is the opposite. So generically these hopping strengths are not equal. This lattice model can either be thought of as a planar model, or a two-layer model where one of the layers is hexagonal and the other layer is triangular. Thus, the c sublattice sites are not symmetry related to the a, b sublattice sites. The a, b sublattice sites may be related by either a $\mathcal{C}_2$ rotation symmetry with any c site as the rotation center, or by a reflection around an axis form by joining a horizontal row of c sites.

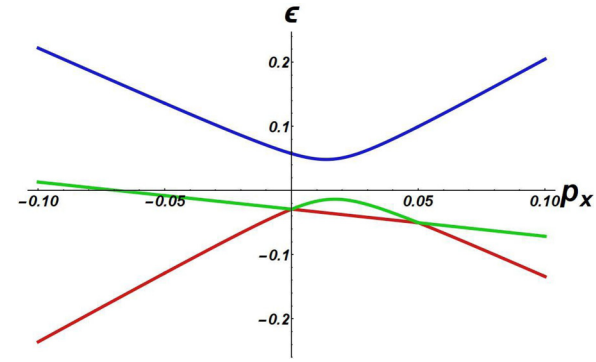

FIG. 8. Case 5 ($n^+ \neq 0$). This figure represents the case where $n^+ < 0$. If we change to $n^+ > 0$ then the bottom band becomes standalone.

A. Tight-binding Hamiltonian

The hopping Hamiltonian that we consider on this graphene-like lattice going by the above symmetry considerations is given by Eq. (23), where n_1, n_2 are unit-cell indices using the primitive lattice vectors of the underlying triangular lattice. Here we are not considering staggered potentials, whose effect is discussed in Sec. III B (in particular case 5: $n^+\tau^0 \otimes \Lambda^8$; a term like $\tau^0 \otimes \Lambda^3$ is ruled out by $\mathcal{C}_2$):

$$\mathcal{H} = \sum_{n_1,n_2} \mathcal{H}_{ab} + \mathcal{H}_{ac} + \mathcal{H}_{bc}, \tag{22}$$

$$\begin{aligned}
\mathcal{H}_{ab} &= -t\,\hat{c}^\dagger_{(n_1,n_2),a}(\hat{c}_{(n_1,n_2),b} + \hat{c}_{(n_1,n_2-1),b} + \hat{c}_{(n_1+1,n_2-1),b}) \\
&\quad + \text{H.c.}, \\
\mathcal{H}_{ac} &= -(t+\delta t_0)\hat{c}^\dagger_{(n_1,n_2),a}\hat{c}_{(n_1,n_2),c} \\
&\quad - (t+\delta t_1)\hat{c}^\dagger_{(n_1,n_2),a}(\hat{c}_{(n_1,n_2-1),c} + \hat{c}_{(n_1+1,n_2-1),c}) + \text{H.c.}, \\
\mathcal{H}_{bc} &= -(t+\delta t_0)\hat{c}^\dagger_{(n_1,n_2),b}\hat{c}_{(n_1,n_2),c} \\
&\quad - (t+\delta t_1)\hat{c}^\dagger_{(n_1,n_2),b}(\hat{c}_{(n_1,n_2+1),c} + \hat{c}_{(n_1-1,n_2+1),c}) + \text{H.c.}
\end{aligned} \tag{23}$$

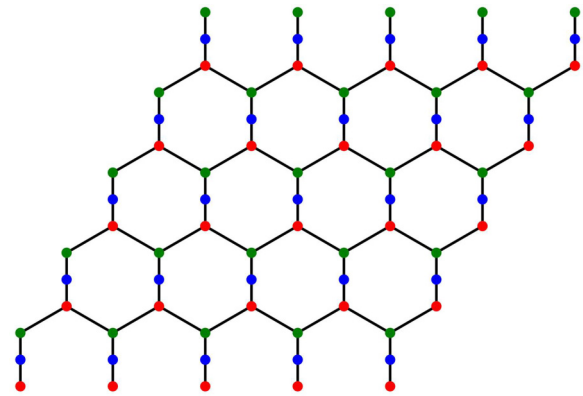

FIG. 9. The graphene-like lattice on which fermions live is shown above. Red points are a sublattice sites, green points are b sublattice points, blue points are c sublattice sites. The underlying Bravais lattice is still triangular the same as graphene.

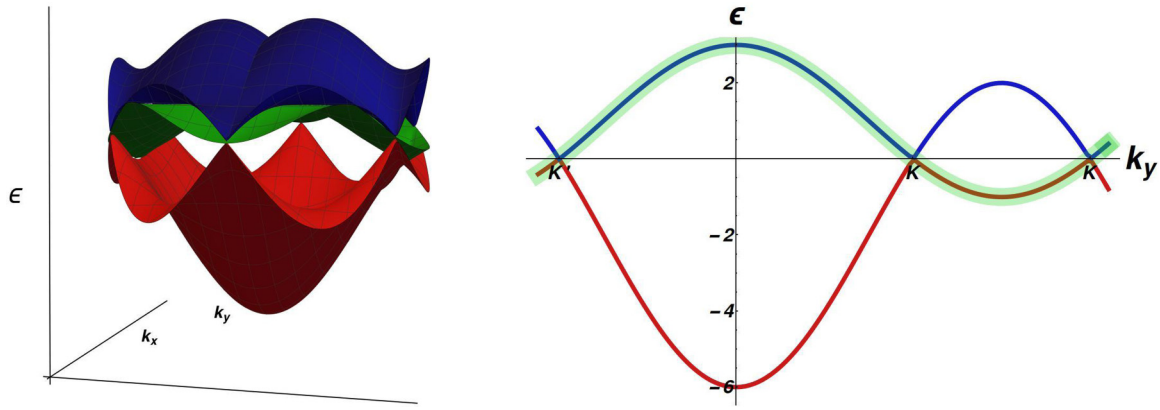

FIG. 10. (Left) Dispersion of the graphene-like lattice Hamiltonian for $\delta t_0 = 0$ and $\delta t_1 = 0$ over the full Brillouin zone. Near the valley points $\vec{K}, \vec{K}'$, they reproduce the continuum band structure of H_μ^{3A} as in Fig. 1. (Right) A cut along $p_y = 0$ is shown to better display the noncontractible loop on which the twofold line degeneracy lives.

This lattice Hamiltonian clearly reproduces the continuum H_μ^{3A} band structure near the valleys $\vec{K}, \vec{K}'$ when the "deformations" δt_0 and δt_1 are zero as may be seen by expanding to leading order near these points in the zone. Essentially they are three copies of graphene hoppings with the same strength. The dispersion over the full Brillouin zone for this choice of parameters is shown in the left panel of Fig. 10. The twofold line degeneracies that connect the two valleys $\vec{K}, \vec{K}'$ form a *noncontractible loop* in the Brillouin zone. This is shown in the right panel of Fig. 10.

For generic deformations, $\delta t_0 \neq 0$, $\delta t_1 \neq 0$, the twofold line degeneracies go away. Then, the continuum Hamiltonians near the two valleys look like

$$\mathcal{H}^{\vec{K}}(\vec{p}) = \frac{\sqrt{3}}{2}(1+\delta t_1)\begin{pmatrix} 0 & \frac{1}{(1+\delta t_1)}(p_x - ip_y) & \frac{2(\delta t_1 - \delta t_0)}{\sqrt{3}(1+\delta t_1)} + (p_x - ip_y) \\ \frac{1}{(1+\delta t_1)}(p_x + ip_y) & 0 & \frac{2(\delta t_1 - \delta t_0)}{\sqrt{3}(1+\delta t_1)} + (p_x + ip_y) \\ \frac{2(\delta t_1 - \delta t_0)}{\sqrt{3}(1+\delta t_1)} + (p_x + ip_y) & \frac{2(\delta t_1 - \delta t_0)}{\sqrt{3}(1+\delta t_1)} + (p_x - ip_y) & 0 \end{pmatrix}, \tag{24}$$

$$\mathcal{H}^{\vec{K}'}(\vec{p}) = \frac{\sqrt{3}}{2}(1+\delta t_1)\begin{pmatrix} 0 & \frac{1}{(1+\delta t_1)}(-p_x - ip_y) & \frac{2(\delta t_1 - \delta t_0)}{\sqrt{3}(1+\delta t_1)} + (-p_x - ip_y) \\ \frac{1}{(1+\delta t_1)}(-p_x + ip_y) & 0 & \frac{2(\delta t_1 - \delta t_0)}{\sqrt{3}(1+\delta t_1)} + (-p_x + ip_y) \\ \frac{2(\delta t_1 - \delta t_0)}{\sqrt{3}(1+\delta t_1)} + (-p_x + ip_y) & \frac{2(\delta t_1 - \delta t_0)}{\sqrt{3}(1+\delta t_1)} + (-p_x - ip_y) & 0 \end{pmatrix}. \tag{25}$$

This deformed Hamiltonian is in the form found in Sec. III, Eq. (21) consistent with all our symmetry considerations. We reiterate that for our lattice hopping model, we have $n^+ = n^- = f^+ = 0$ in the notation of Sec. III. The reasons are as follows: (a) n^+ and n^- are zero because there are no staggered chemical potentials and no intercell same sublattice hoppings. (b) $f^+ = 0$ because we are measuring deformations in hopping with respect to *ab* hoppings within the unit cell. Second, $l_1^+ \neq 0$ is the way we chose to organize the deformations due to δt_0, δt_1 as shown in Eqs. (24) and (25). Therefore, the rest of the Hamiltonian is the undeformed case, which makes $f^- = g^-$ and $m_2^- = l_1^-$. In fact, $f^- = g^-$ is precisely what happens in graphene.

The band structure for this generic case ($\delta t_0 \neq \delta t_1 \neq 0$) near the valleys is shown in Fig. 11. We find that the bottom two bands touch linearly as in a Dirac cone, while the middle and the top band involve two Dirac cones. The dispersion along the line connecting the two Dirac cones is rather flat. This is basically the lattice realization of case 3 in Sec. III where the line connecting the two Dirac cones is completely flat. The lack of complete flatness for the lattice case is due to subleading terms.

For the middle and bottom band, there can in fact be another Dirac cone apart from the one mentioned above, which can annihilate with a similar counterpart from the other valley as we tune δt_1 for a given δt_0 as shown in Fig. 12. This happens when δt_1 and δt_0 are of the same sign. When their signs are opposite, they are always annihilated as shown in Fig. 13. In our graphene-like lattice, we expect the opposite

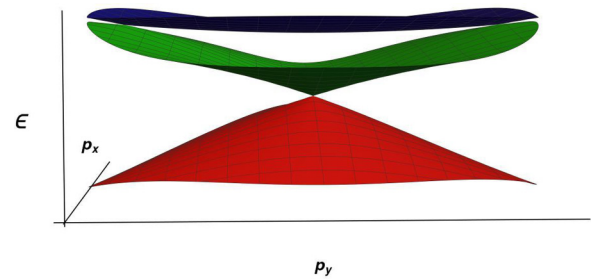

FIG. 11. For $\delta t_0 = 0.5$ and $\delta t_1 = -0.25$ the dispersion has this behavior where the bottom band and the middle band has one Dirac point and the middle band and the top band has two Dirac points.

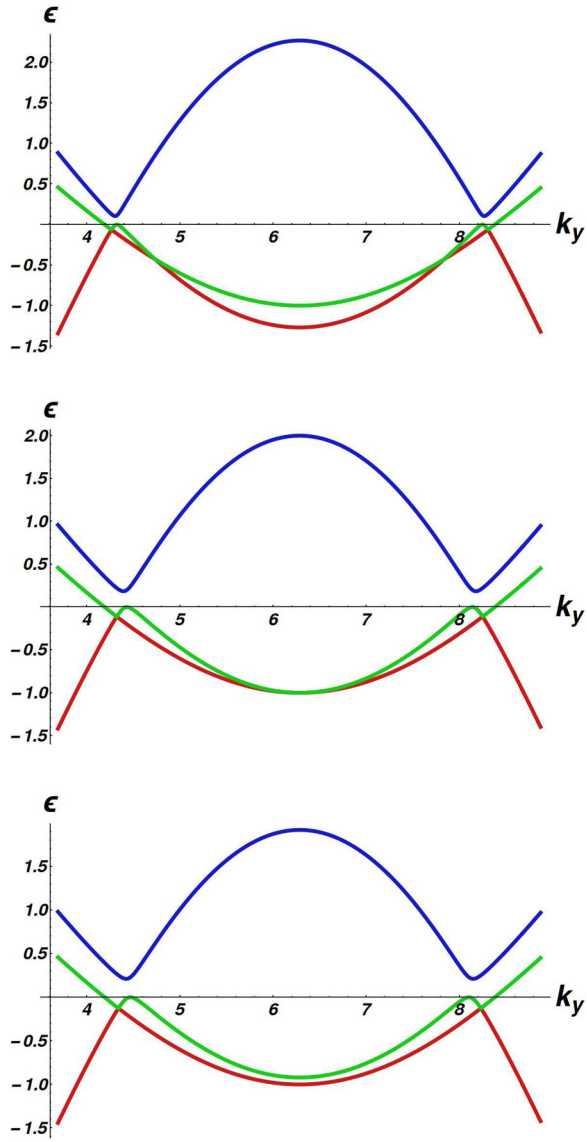

FIG. 12. Three figures are for $\delta t_0 = 0.5$ and $\delta t_1 = 0.35.0.25, 0.22$, respectively. As we see here the extra Dirac point travels and gets finally gapped out.

sign case to be the physical case if we assume that hopping strength decreases with distance.

We also mention a fine-tuned case of deformation when $\delta t_0 = \delta t_1 \neq 0$. The corresponding band structure near the valleys is included in case 2 in Sec. III where we again have a threefold degeneracy without twofold line degeneracies. A final comment on breaking the $\mathcal{C}_2$ symmetry and thereby opening gaps near the Dirac cones: this makes the gapped bands topologically trivial bands with zero Chern number just like graphene.

B. Effect of magnetic field

To conclude this section, we quickly discuss the Landau levels of our lattice model in the presence of a perpendicular magnetic field which is mainly a numerical study. The Landau level structure of graphene and its multilayer variants [7] have

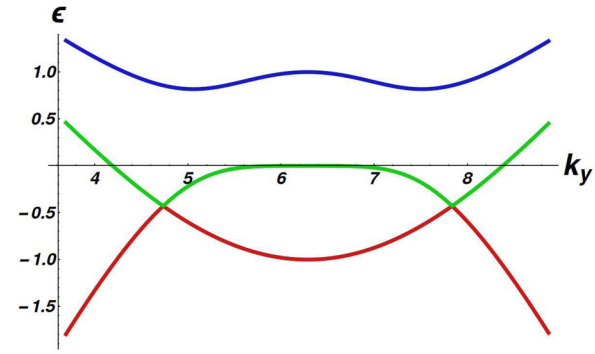

FIG. 13. For $\delta t_0 = 0.5$ and $\delta t_1 = -0.25$ the dispersion has this behavior along $k_y = 0$ line.

received attention due to their different quantization properties than the 2D electron gas. This motivates us to discuss the Landau levels in our case because of the presence of the nonstandard "three-band" Dirac cone structures as discussed previously.

We start by showing our numerical computation of the Landau levels in the Hofstadter limit for our model with hopping deformations for a very large $q = 1000$ in Fig. 14. We can identify regions in this diagram that are linear where the underlying band is dominantly quadratic (e.g., near the very bottom and top of the three bands), and regions that are square-root like where the underlying band is dominantly linear (e.g. near Dirac cones). These features are marked in Fig. 14. In the region where the top band and middle band touch with two separate Dirac cones, we find that the behavior is neither linear nor square-root like. Numerically fitting this behavior gave us a power close to 7/9.

Going by the usual steps at the continuum level, we run into difficulty. For example, for the case of H_K^{3A}, we arrive at a Landau level Hamiltonian that is proportional to $\begin{pmatrix} 0 & \hat{a}^\dagger & \hat{a}^\dagger \\ \hat{a} & 0 & \hat{a} \\ \hat{a} & \hat{a}^\dagger & 0 \end{pmatrix}$ where $\hat{a} = \frac{l_B^2}{2\hbar}\mathbb{P}_+$ and $\hat{a}^\dagger = \frac{l_B^2}{2\hbar}\mathbb{P}_-$, $\mathbb{P}_+ = (p_x + eBy) + ip_y$ and $\mathbb{P}_- = (p_x + eBy) - ip_y$ and $[\mathbb{P}_+, \mathbb{P}_-] = \frac{2\hbar}{l_B^2}$. It is not clear how to derive the Landau level quantization starting with this. One may however attempt to do a semiclassical analysis [41,42] when $\delta t_0 > 0$ and $\delta t_1 < 0$ (nonzero deformation of hopping) such that there are well defined closed electron orbits. This is

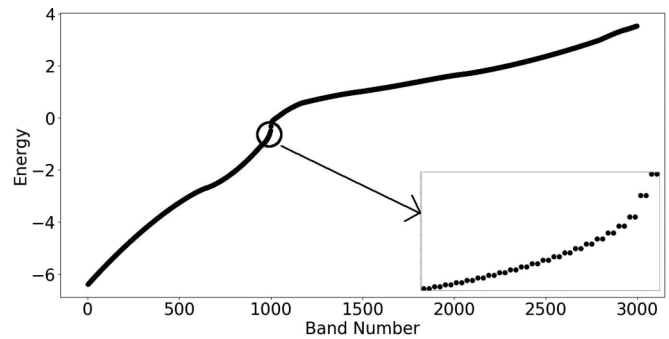

FIG. 14. Here we present the spectrum for $\delta t_0 = 0.5$, $\delta t_1 = -0.25$ where $p = 1, q = 1000$. In the inset it shows that for the bottom band the spectrum is $\sim\sqrt{n}$ and they are doubly degenerate.

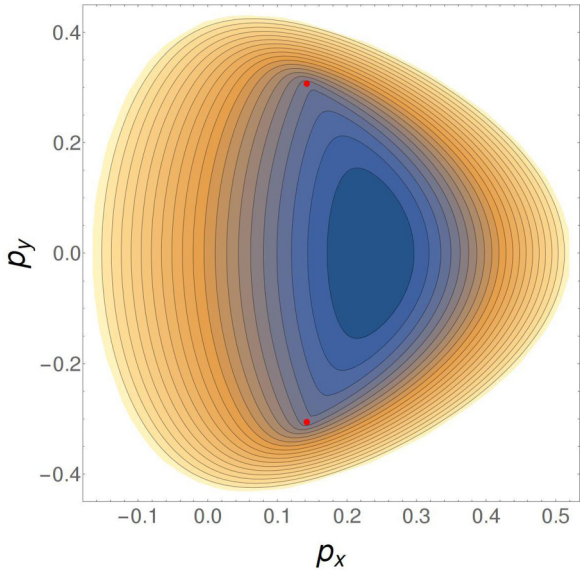

FIG. 15. Orbit of the electron in the top band near the two same energy band degeneracy for the top band. The red points signify the location of the Dirac points.

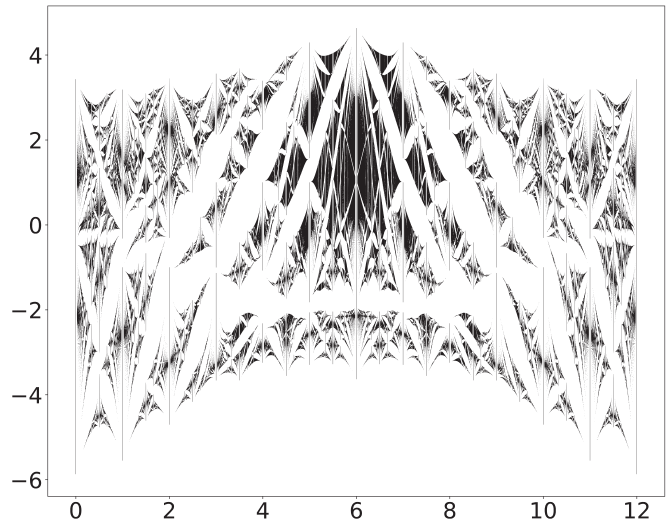

FIG. 16. Hofstadter butterfly for our model lattice with $\delta t_0 = 0.1$ and $\delta t_1 = -0.1$. Here x axis represents the flux in units of quantum flux enclosed by the unit cell and the y axis represents the energy.

asymptotically valid for $n \gg 1$. For regions where the band structure is quadratic/linear, this formula will yield the usual behaviors of n and $\sqrt{n}$, respectively, as also seen in our numerical computations (Fig. 14). The numerical results have been obtained by diagonalizing the Hofstadter problem for very large q, equivalently for very small magnetic fields.

Near the unusual two Dirac cone structure between the top and middle band, the orbits have nonstandard shapes as shown in Fig. 15 with the left side scaling linearly in energy, while the right side scaling quadratically in energy. Crudely estimating the area of such orbits leads to the conclusion that Landau level behavior will be somewhere in between n (coming from quadratic scaling part of the orbit) and $\sqrt{n}$ (coming from the linear scaling part of the orbit). However, it does not yield a neat power law, but since the semiclassical analysis is applicable only in the $n \gg 1$ limit, we may guess that the numerical observation of $\sim 7/9$ exponent is due to the quadratic scaling part of the orbit eventually dominating the orbited area.

We finally show the full Hofstadter butterfly spectrum for our lattice model in Fig. 16 for completeness. Here we can identify a few features of our lattice model: (1) the Hofstadter butterfly repeats after 12 quantum flux per unit cell. This is due to the fact that in our graphene-like lattice model, the smallest area covered by the hopping is not the hexagonal plaquette, but $\frac{1}{12}$th of it. (2) There is no particle hole symmetry. (3) For $\frac{1}{2}$ flux quanta per smallest area, the model still has time reversal symmetry and thus there is no gap.

V. CONCLUSION AND OUTLOOK

In summary, the central result of this paper is the continuum Hamiltonian H_K^{3A} [Eq. (3)] and its eigensystem [Eq. (4)] that we wrote down as a three-band generalization of the 2D Dirac Hamiltonian. We were led to consider them in order to arrive at a beyond-Dirac-like or non-SU(2) geometric phase structure in two dimensions as our primary motivation (Sec. I). We exposed the geometric phase structure of H_K^{3A} using a triplet of indices as described in Sec. II and summarized in Table I. Through this table, we see how H_K^{3A} contrasts with other cases that have SU(2) geometric phase structure.

Guided by the SU(3) nature of H_K^{3A}, we constructed in Sec. III the general family of continuum 2D Hamiltonians [Eq. (21)] with fermions (at a valley) in the SU(3) fundamental representation, which is allowed by time reversal $\mathcal{T}$ symmetry, and the space symmetries of inversion $\mathcal{C}_2$ and reflections $\mathcal{P}_x$, $\mathcal{P}_y$. H_K^{3A} sits at a special point in this family of Hamiltonians. We further categorized the various three-band dispersions that result from different regions in this family of Hamiltonians (Sec. III B).

In Sec. IV we provided a tight-binding lattice model realization of H_K^{3A} on a graphene-like lattice (Fig. 9), where the three bands touch each other at K and K' when the hopping matrix elements are appropriately fine tuned, with a line of twofold degeneracy connecting K and K' on a noncontractible loop in the Brillouin zone (right panel of Fig. 10). Away from the fine-tuned point, we realize various cases of Eq. (21). We studied the effect of a uniform magnetic field including its Hofstadter butterfly (Fig. 16) and found that the Landau level quantization is different for different parts of the spectrum (Fig. 14).

We end the summary with a conceptual remark. Our discussion on the geometric phase structure of the H_K^{3A} [Eq. (3)] in Sec. II shows that there is a way to construct a topological invariant in the presence of line degeneracies. Often, geometric phases in two dimensions are discussed by considering a closed orbit around some point degeneracy, chosen such that the (restricted) one-dimensional band structure on the orbit is *gapped* throughout. The winding number of the wave function's phase in this restricted dimension then serves as a topological invariant that characterizes the geometric phase structure around the point degeneracy in the higher dimension [43]. Here we have shown that there is a way to generalize this approach for a threefold point degeneracy

in two dimensions with line degeneracies, and thereby no adiabaticity in the sense of Berry [3]. As discussed in the text [Eq. (4) and paragraph below], analytical continuation of the eigenvalues and eigenvectors on a one-dimensional loop *across* the line degeneracy while considering a closed orbit around the threefold point degeneracy (Fig. 2) is what allows for this generalization. This idea of analytical continuation is then used—*and may be used more generally in other situations*—for an appropriate topological invariant characterization of the geometric phase structure in the restricted dimension even in the presence of *gapless* points. This may be considered as a new lens on the discussion of geometric phase structure of two-dimensional band structures, and possibly in higher dimensions, e.g., giving a perspective on some recent striking three-dimensional band structures [29,44] whose cuts in two dimensions harbor threefold point degeneracies with emanating twofold line degeneracies as well.

In the future it will be interesting to pursue the following lines of research motivated by this paper. We have mainly explored three-band generalizations with two valleys. However, for three or higher bands it is not obvious if there are generalized band structures which accommodate more than two valleys in some interesting way. For example, in graphene in the presence of a uniform perpendicular magnetic field, it is known that there can be any even number of Dirac points [45]. Perhaps for SU(3), something similar might be possible even in the absence of magnetic fields including an odd number of valleys. We have not paid attention to the spin quantum number in this paper. One can study what new kind of terms can arise in the sense of Eq. (21) in the presence of spin-orbit coupling. In the presence of more bands, can one realize higher representations of SU(3) as well as other SU($N > 3$). Apart from these questions of the "band engineering" kind, there is the important question with regards to the effect of interaction terms allowed by symmetries on these band structures, as also the question regarding the physical consequences of such threefold band structures such as in measurements of optical conductivity [46,47], magnetotransport [22,48], and atomic collapse [49].

Finally, we ask ourselves where can we see our imagined noninteracting band structures in nature. Apart from the electronic structure on a possible graphene-like lattice, perhaps other platforms like photonic band systems [50,51], cold atomic systems [52–55], or designed lattice systems [56,57] may be interesting platforms to search for this. It remains to be seen if the beyond-Dirac-like geometric phase structure that we studied in this paper can be observed in some 2D layered material system.

ACKNOWLEDGMENTS

We thank G. Murthy and Luiz Henrique Santos for some discussions. S.P. thanks the support of NSF Grant DMR-1056536 during the initial conception stages. S.P. thanks the IRCC, IIT Bombay (17IRCCSG011) for financial support, and the hospitality of Dept. of Physics and Astronomy, University of Kentucky where part of the work was completed. A.D. thanks to the support of NSF Grant No. DMR-1611161 and NSF Grant No. DMR-1306897. This research was supported in part by the International Center for Theoretical Sciences (ICTS) during a visit for participating in the program The 2nd Asia Pacific Workshop on Quantum Magnetism (Code: ICTS/apfm2018/11).

[1] D. Vanderbilt, *Berry Phases in Electronic Structure Theory: Electric Polarization, Orbital Magnetization and Topological Insulators* (Cambridge University Press, Cambridge, 2018).
[2] D. Xiao, M.-C. Chang, and Q. Niu, Rev. Mod. Phys. **82**, 1959 (2010).
[3] M. V. Berry, Proc. R. Soc. London Ser. A **392**, 45 (1984).
[4] D. J. Thouless, M. Kohmoto, M. P. Nightingale, and M. den Nijs, Phys. Rev. Lett. **49**, 405 (1982).
[5] O. Vafek and A. Vishwanath, Annu. Rev. Condens. Matter Phys. **5**, 83 (2014).
[6] Y. Zhang, Z. Jiang, J. P. Small, M. S. Purewal, Y.-W. Tan, M. Fazlollahi, J. D. Chudow, J. A. Jaszczak, H. L. Stormer, and P. Kim, Phys. Rev. Lett. **96**, 136806 (2006).
[7] K. S. Novoselov, E. McCann, S. V. Morozov, V. I. Fal'ko, M. I. Katsnelson, U. Zeitler, D. Jiang, F. Schedin, and A. K. Geim, Nat. Phys. **2**, 177 (2006).
[8] A simple example is a quantum spin-$\frac{1}{2}$ $\hat{\mathbf{S}}$ in an external (classical) magnetic field $H = \mathbf{B} \cdot \hat{\mathbf{S}}$.
[9] For example, in graphene, space inversion and time reversal get rid of one of the parameters [5].
[10] The wave functions in fact do not return to themselves when the parameter completes a circuit, unlike the usual case in any (Abelian) Berry phase calculation.
[11] C.-H. Park and N. Marzari, Phys. Rev. B **84**, 205440 (2011).
[12] Z. Lin and Z. Liu, J. Chem. Phys. **143**, 214109 (2015).
[13] B. Bradlyn, J. Cano, Z. Wang, M. G. Vergniory, C. Felser, R. J. Cava, and B. A. Bernevig, Science **353**, aaf5037 (2016).
[14] D. Green, L. Santos, and C. Chamon, Phys. Rev. B **82**, 075104 (2010).
[15] B. Dóra, J. Kailasvuori, and R. Moessner, Phys. Rev. B **84**, 195422 (2011).
[16] Z. Lan, N. Goldman, A. Bermudez, W. Lu, and P. Öhberg, Phys. Rev. B **84**, 165115 (2011).
[17] D. F. Urban, D. Bercioux, M. Wimmer, and W. Häusler, Phys. Rev. B **84**, 115136 (2011).
[18] J. Wang, H. Huang, W. Duan, and Z. Liu, J. Chem. Phys. **139**, 184701 (2013).
[19] A. Raoux, M. Morigi, J.-N. Fuchs, F. Piéchon, and G. Montambaux, Phys. Rev. Lett. **112**, 026402 (2014).
[20] G. Giovannetti, M. Capone, J. van den Brink, and C. Ortix, Phys. Rev. B **91**, 121417(R) (2015).
[21] G. Palumbo and K. Meichanetzidis, Phys. Rev. B **92**, 235106 (2015).
[22] Y. Xu and L.-M. Duan, Phys. Rev. B **96**, 155301 (2017).
[23] L. Wang and D.-X. Yao, Phys. Rev. B **98**, 161403(R) (2018).
[24] B. Q. Lv, Z.-L. Feng, Q.-N. Xu, X. Gao, J.-Z. Ma, L.-Y. Kong, P. Richard, Y.-B. Huang, V. N. Strocov, C. Fang *et al.*, Nature (London) **546**, 627 (2017).

[25] G. W. Winkler, Q. S. Wu, M. Troyer, P. Krogstrup, and A. A. Soluyanov, Phys. Rev. Lett. **117**, 076403 (2016).
[26] H. Weng, C. Fang, Z. Fang, and X. Dai, Phys. Rev. B **93**, 241202(R) (2016).
[27] Z. Zhu, G. W. Winkler, Q. S. Wu, J. Li, and A. A. Soluyanov, Phys. Rev. X **6**, 031003 (2016).
[28] H. Weng, C. Fang, Z. Fang, and X. Dai, Phys. Rev. B **94**, 165201 (2016).
[29] G. Chang, S.-Y. Xu, S.-M. Huang, D. S. Sanchez, C.-H. Hsu, G. Bian, Z.-M. Yu, I. Belopolski, N. Alidoust, H. Zheng *et al.*, Sci. Rep. **7**, 1688 (2017).
[30] I. C. Fulga and A. Stern, Phys. Rev. B **95**, 241116(R) (2017).
[31] G. Chang, S.-Y. Xu, B. J. Wieder, D. S. Sanchez, S.-M. Huang, I. Belopolski, T.-R. Chang, S. Zhang, A. Bansil, H. Lin *et al.*, Phys. Rev. Lett. **119**, 206401 (2017).
[32] C. Zhong, Y. Chen, Z.-M. Yu, Y. Xie, H. Wang, S. A. Yang, and S. Zhang, Nat. Commun. **8**, 15641 (2017).
[33] J. Yu, B. Yan, and C.-X. Liu, Phys. Rev. B **95**, 235158 (2017).
[34] X. Zhang, Z.-M. Yu, X.-L. Sheng, H. Y. Yang, and S. A. Yang, Phys. Rev. B **95**, 235116 (2017).
[35] H. Yang, J. Yu, S. S. P. Parkin, C. Felser, C.-X. Liu, and B. Yan, Phys. Rev. Lett. **119**, 136401 (2017).
[36] P. R. Wallace, Phys. Rev. **71**, 622 (1947).
[37] Essentially, H_K^{3B} is equivalent to $\mathbf{B}\cdot\hat{\mathbf{S}}$ for a quantum spin-1 in an external (classical) magnetic field that is confined to a plane.
[38] F. Halzen and A. D. Martin, *Quarks and Leptons: An Introductory Course in Modern Particle Physics* (Wiley, New York, 1984).
[39] In terms of the triplet of indices introduced in Sec. II, this twofold degeneracy gets classified as 1 ($\theta'_{\mathbf{p}}$), 1 (H) and 0(t), 2(m), 2(b), where the prime on $\theta'_{\mathbf{p}}$ is to point out that the circuit is made near this twofold degeneracy which is not at the origin.
[40] G. P. Mikitik and Y. V. Sharlai, Phys. Rev. B **77**, 113407 (2008).
[41] J. N. Fuchs, F. Piéchon, M. O. Goerbig, and G. Montambaux, Eur. Phys. J. B **77**, 351 (2010).
[42] A. Yu Ozerin and L. A. Falkovsky, Phys. Rev. B **85**, 205143 (2012).
[43] S. Ryu, A. P. Schnyder, A. Furusaki, and A. W. W. Ludwig, New J. Phys. **12**, 065010 (2010).
[44] C. K. Barman, C. Mondal, B. Pathak, and A. Alam, Phys. Rev. B **99**, 045144 (2019).
[45] J.-W. Rhim and K. Park, Phys. Rev. B **86**, 235411 (2012).
[46] E. Illes and E. J. Nicol, Phys. Rev. B **94**, 125435 (2016).
[47] A. D. Kovács, G. Dávid, B. Dóra, and J. Cserti, Phys. Rev. B **95**, 035414 (2017).
[48] SK Firoz Islam and P. Dutta, Phys. Rev. B **96**, 045418 (2017).
[49] E. V. Gorbar, V. P. Gusynin, and D. O. Oriekhov, Phys. Rev. B **99**, 155124 (2019).
[50] C. M. Soukoulis (Ed.) *Photonic Crystals and Light Localization in the 21st Century* (Springer, Netherlands, 2001).
[51] S. Ray, A. Ghatak, and T. Das, Phys. Rev. B **95**, 165425 (2017).
[52] M. Lewenstein, A. Sanpera, V. Ahufinger, B. Damski, A. Sen(De), and U. Sen, Adv. Phys. **56**, 243 (2007).
[53] L. Tarruell, D. Greif, T. Uehlinger, G. Jotzu, and T. Esslinger, Nature (London) **483**, 302 (2012).
[54] H. Hu, J. Hou, F. Zhang, and C. Zhang, Phys. Rev. Lett. **120**, 240401 (2018).
[55] H. Hu and C. Zhang, Phys. Rev. A **98**, 013627 (2018).
[56] A. Tadjine, G. Allan, and C. Delerue, Phys. Rev. B **94**, 075441 (2016).
[57] M. R. Slot, S. N. Kempkes, E. J. Knol, W. M. J. van Weerdenburg, J. J. van den Broeke, D. Wegner, D. Vanmaekelbergh, A. A. Khajetoorians, C. Morais Smith, and I. Swart, Phys. Rev. X **9**, 011009 (2019).